

Generation of isolated attosecond pulses in the far field by spatial filtering with an intense few-cycle mid-infrared laser

Cheng Jin, Anh-Thu Le, Carlos A. Trallero-Herrero, and C. D. Lin

J. R. Macdonald Laboratory, Physics Department, Kansas State University, Manhattan, Kansas 66506-2604, USA

(Received 18 July 2011; published 10 October 2011)

We report theoretical calculations of high-order harmonic generation (HHG) of Xe with the inclusion of multielectron effects and macroscopic propagation of the fundamental and harmonic fields in an ionizing medium. By using the time-frequency analysis we show that the reshaping of the fundamental laser field is responsible for the continuum structure in the HHG spectra. We further suggest a method for obtaining an isolated attosecond pulse (IAP) by using a filter centered on axis to select the harmonics in the far field with different divergence. We also discuss the carrier-envelope-phase dependence of an IAP and the possibility to optimize the yield of the IAP. With intense few-cycle mid-infrared lasers, this offers a possible method for generating isolated attosecond pulses.

DOI: [10.1103/PhysRevA.84.043411](https://doi.org/10.1103/PhysRevA.84.043411)

PACS number(s): 42.65.Ky, 42.65.Re, 42.65.Jx, 31.70.Hq

I. INTRODUCTION

High-order harmonic generation (HHG), one of the most interesting nonlinear phenomena occurring when atoms or molecules are exposed to an intense infrared laser field, has been widely used for the production of attosecond pulses in the extreme ultraviolet (xuv) [1–5]. Due to its great potential for probing ultrafast electronic processes, different methods have been used to generate isolated attosecond pulses (IAPs). Using carrier-envelope-phase (CEP) stabilized few-cycle laser pulses, an IAP as short as 80 attoseconds has been generated by synthesizing harmonics beyond the cutoff [6,7]. Starting with elliptically polarized light, the polarization gating technique in which HHG emission from the central cycle of the pulse is selected, has also produced an isolated 130 as pulse [8,9]. In a tight-focusing geometry, using the so-called spatiotemporal gating, an IAP can be generated since different phase-matching conditions can be achieved for different ranges of harmonics [10,11]. Other alternative methods of IAP generation have been reported, including confining harmonics generated in a narrow temporal window in the leading edge of a laser pulse, where a 210 as IAP has been reported [12]. IAPs can also be generated by optimizing the pressure and length of the gas cell [13–15] or by using a spatial filter in the far field [16–18]. Indeed, there is a plethora of techniques for the production of IAPs, with the idea that harmonics can be generated from only half an optical cycle in a few- or multicycle infrared laser pulse.

Since the harmonic field generated by all atoms or molecules within the laser focus copropagates with the fundamental laser field in the medium, as well as possible further propagation in free space depending on the experimental setup, the understanding of the observed HHG consists of two parts: first, the HHG emission from individual atoms (or molecules) through the laser-induced dipole; second, the propagation of the fundamental and harmonic fields in the medium and in free space. There are two fundamental equations to be solved: the time-dependent Schrödinger equation (TDSE) for the single-atom (or single-molecule) response, and Maxwell's wave equation for the propagation process. In practice, in the first step, the solution of TDSE is normally not employed due to computational difficulties. Instead, the strong-field

approximation (SFA) (or Lewenstein model) [19] is used. However, it is well known that the SFA fails to reproduce the observed HHG spectra and thus the reliability of the predicted spectra after propagation in the medium is questionable. In recent years, a quantitative rescattering (QRS) theory has been proposed by our group [20–22], which has been corroborated subsequently by others [23–29]. The single-atom (or single-molecule) response obtained from QRS has been shown to be as accurate as the one from TDSE, but the calculation is as easy as the SFA whenever photoionization dipole matrix elements can be readily calculated. Taking advantage of this theoretical success, we have recently incorporated the QRS theory into the macroscopic propagation of harmonic fields in the medium. To this point, we have shown that QRS-based macroscopic harmonic spectra (i) agree well with TDSE-based HHG spectra for Ar [30] and (ii) compare well with experimental HHG spectra reported for Ar, N₂, and CO₂ [31–33] when the experimental conditions are well specified. It has been demonstrated that this approach can be used to calculate macroscopic HHG spectra by polyatomic molecules [34] even though the predictions have not been tested yet against experiments. Outside of our group, the QRS theory has been applied to study HHG by the two-color fields in which the propagation effect is included [35]. These applications of QRS theory are focused on HHG spectra. In this paper, we focus on the analysis of attosecond pulse generation which inevitably tests the phases of the harmonics obtained in our simulation.

Recently, Xe has become a favorite candidate for generating intense IAPs [36], studying phase-matching effects in the generation of high-energy photons [37], and probing multielectron dynamics with high-harmonic spectroscopy [38]. Ferrari *et al.* [36] reported the generation of a high-energy 160 as IAP using low-order harmonics of Xe from a CEP-stabilized laser. They used very high laser intensity and very dilute gas so that the fundamental field was not severely distorted, but the atomic ground state was depleted very quickly in the leading edge of the laser pulse. Only low-order harmonics emitted within one half cycle were used to obtain an IAP. Shiner *et al.* [38] used a 1.8 μm laser with a duration of less than two optical cycles to obtain the HHG spectra of Xe up to

the photon energy of 160 eV. They have shown that HHG spectra exhibited strong enhancement above about 90 eV. This enhancement is well known in photoionization (PI) of Xe due to the presence of a strong shape resonance from the $4d$ shell which, through channel coupling, modifies the partial PI cross section of the $5p$ shell of Xe—a feature attributed to many-electron effects. According to QRS, such an enhancement is anticipated since the partial photorecombination (PR) cross section (related to photoionization) enters directly into the laser-induced dipole. To simulate HHG spectra at high photon energies, multielectron effects on the laser-induced dipoles have to be included. Using such dipoles in QRS, we simulate the HHG spectra of Xe generated by $1.8 \mu\text{m}$ lasers by including macroscopic propagation effects.

In Shiner *et al.* [38], HHG spectra from Xe have been reported for laser intensities from 0.54 to $2.14 \times 10^{14} \text{ W/cm}^2$ (see Fig. 7 of the supplement of that paper). They showed that the HHG spectra of Xe had the same energy dependence as the photoionization cross sections of Xe when the laser intensities are higher than about $1.45 \times 10^{14} \text{ W/cm}^2$. According to QRS, this implies that, at high intensities, the wave packet [see Eq. (11) below] is flat. At these high intensities the fundamental laser field is severely modified as it propagates in the medium; thus, the harmonic spectra cannot be attributed directly to the coherent emission from all the target atoms under the constant field of the incident beam. The validity of a flat-wave-packet assumption under the experimental conditions of Shiner *et al.* [38] will be studied separately elsewhere. In this paper we focus on another issue seen in Ref. [38]; namely, the observation that the HHG spectra exhibit nearly continuous photon energy distributions (to be called continuum structure) at high laser intensities. Such a continuum structure was later observed in Xe again at a different gas pressure and also in other molecules like NO [39]. Our goal in this paper is to demonstrate that isolated attosecond pulses are generated by these continuum harmonics. For this, we demonstrate how to select different ranges of harmonics to synthesize an IAP by using a spatial filter in the far field. This approach is different from that in Ferrari *et al.* [36], but similar to the analysis in Gaarde *et al.* [17].

The rest of this paper is arranged as follows: In Sec. II, we briefly summarize the propagation equations, wavelet theory for the time-frequency analysis, formulas for the attosecond pulse generation, and QRS theory including multielectron effects. In Sec. III, the theoretical results are presented and analyzed for different experimental conditions for IAPs by synthesizing harmonic orders from 40 to 80 (H40-H80) and H90-H130. We also compare attosecond pulses calculated using QRS and the SFA. An analysis of CEP dependence of the generated IAP presented at the end of this section concludes that it is still possible to obtain an IAP even for lasers where the CEP is not stabilized. A short summary in Sec. IV concludes this paper.

II. THEORETICAL METHODS

A. Propagation equations of fundamental and harmonic fields

The propagation of the fundamental laser field and high harmonics in an ionizing medium has been described in detail in Ref. [32], so we only recall the main equations here. The

evolution of the fundamental field is described by a three-dimensional (3D) Maxwell wave equation [40,41]:

$$\nabla^2 E_1(r,z,t) - \frac{1}{c^2} \frac{\partial^2 E_1(r,z,t)}{\partial t^2} = \mu_0 \frac{\partial J_{\text{abs}}(r,z,t)}{\partial t} + \frac{\omega_0^2}{c^2} (1 - \eta_{\text{eff}}^2) E_1(r,z,t), \quad (1)$$

where $E_1(r,z,t)$ is the transverse electric field with central frequency ω_0 . $\nabla^2 = \nabla_\perp^2 + \partial^2 / \partial z^2$ in cylindrical coordinates, where z is the axial propagation direction. The effective refractive index is

$$\eta_{\text{eff}}(r,z,t) = \eta_0(r,z,t) + \eta_2 I(r,z,t) - \frac{\omega_p^2(r,z,t)}{2\omega_0^2}. \quad (2)$$

The linear term $\eta_0 = 1 + \delta_1 - i\beta_1$ accounts for refraction (δ_1) and absorption (β_1) by the neutral atoms, the second term describes the optical Kerr nonlinearity which depends on the instantaneous laser intensity $I(t)$, and the third term contains the plasma frequency $\omega_p = [e^2 n_e(t) / (\epsilon_0 m_e)]^{1/2}$, where m_e and e are the mass and charge of an electron, respectively, and $n_e(t)$ is the density of free electrons. The absorption term $J_{\text{abs}}(t)$ due to the ionization of the medium is given by [4,42]

$$J_{\text{abs}}(t) = \frac{\gamma(t) n_e(t) I_p E_1(t)}{|E_1(t)|^2}, \quad (3)$$

where $\gamma(t)$ is the ionization rate and I_p is the ionization potential. Ionization rates involved in Eq. (3) and in free electron density $n_e(t)$ are calculated using the improved Ammosov-Delone-Krainov (ADK) theory [43]. The fundamental laser field is assumed to be Gaussian both in space and time at the entrance of the medium, and the gas pressure is constant within the medium.

The 3D propagation equation of the harmonic field is [4,44,45]

$$\nabla^2 E_h(r,z,t) - \frac{1}{c^2} \frac{\partial^2 E_h(r,z,t)}{\partial t^2} = \mu_0 \frac{\partial^2 P(r,z,t)}{\partial t^2}, \quad (4)$$

where $P(r,z,t)$ is the polarization depending on the applied fundamental field $E_1(r,z,t)$. Here the free-electron dispersion is neglected because the frequencies of high harmonics are much higher than the plasma frequency. In general, the polarization $P(r,z,t)$ is separated into linear and nonlinear components, and the linear susceptibility $\chi^{(1)}(\omega)$ includes both linear dispersion and absorption effects of the harmonics [46]. The nonlinear polarization term $P_{\text{nl}}(r,z,t)$ can be expressed as

$$P_{\text{nl}}(r,z,t) = [n_0 - n_e(r,z,t)] D(r,z,t), \quad (5)$$

where $n_0 - n_e(r,z,t)$ gives the density of the remaining neutral atoms, and $D(r,z,t)$ is the single-atom-induced dipole moment. Note that Eqs. (1) and (4) are solved by using the Crank-Nicholson routine in the frequency domain.

Once the harmonic field at the exit face (near field) of the medium is computed, the harmonics propagating in free space in the far field can be obtained from near-field harmonics through a Hankel transformation [47–49].

B. Wavelet analysis of attosecond pulses

A time-frequency representation (TFR) (or spectrogram) of the harmonic field $E_h(t)$ is a simultaneous representation of

the temporal and spectral characteristics of the harmonics. We perform the time-frequency analysis in terms of the wavelet transform of the harmonic field [50–53]:

$$A(t, \omega) = \int E_h(t') w_{t, \omega}(t') dt', \quad (6)$$

with the wavelet kernel $w_{t, \omega}(t') = \sqrt{\omega} W[\omega(t' - t)]$. We choose the Morlet wavelet [50]:

$$W(x) = (1/\sqrt{\tau}) e^{ix} e^{-x^2/2\tau^2}. \quad (7)$$

The width of the window function in the wavelet transform varies as the frequency changes, but the number of oscillations (proportional to τ) within the window is held constant. The dependence of $A(t, \omega)$ on the parameter τ has been tested. The absolute value of $A(t, \omega)$ depends on τ , but the general temporal pattern does not change much. In this paper, we choose $\tau = 15$ to perform the wavelet transform.

Harmonics emitted at the exit plane (near field) of the medium act as a source for the far-field harmonics. In order to avoid the complexity of the harmonic spatial distribution in the near field (see Fig. 4 in Ref. [32]), we calculate $A(t, \omega)$ for each radial point in the near field and then integrate over the radial coordinate [52]:

$$|A_{\text{near}}(t, \omega)|^2 = \int_0^\infty 2\pi r dr \left| \int E_h(r, t') w_{t, \omega}(t') dt' \right|^2. \quad (8)$$

To demonstrate the divergence of the harmonics, we preform the TFR for each radial point in the far field.

The spectral filter used to select a range of harmonics (ω_1 – ω_2) could affect the generation of attosecond pulse trains (APTs) or IAPs. Theoretically we can obtain the total intensity of an APT or an IAP in the near field as follows [54]:

$$I_{\text{near}}(t) = \int_0^\infty 2\pi r dr \left| \int_{\omega_1}^{\omega_2} E_h(r, \omega) e^{i\omega t} d\omega \right|^2. \quad (9)$$

In the far field, a spatial filter is used to select the harmonics in a prescribed area. In this paper, we assume that the filter is circular with a radius r_0 and is perpendicular to the propagation direction of the harmonics. The intensity of an APT or an IAP in the far field is

$$I_{\text{far}}(t) = \int_0^{r_0} 2\pi r dr \left| \int_{\omega_1}^{\omega_2} E_h^f(r, \omega) e^{i\omega t} d\omega \right|^2. \quad (10)$$

C. Photorecombination dipole moment of Xe in QRS theory

The single-atom-induced dipole moment $D(t)$ in Eq. (5) is obtained by QRS theory. It can be expressed in the energy (or frequency) domain as follows [22,55]:

$$D(\omega) = W(\omega)d(\omega), \quad (11)$$

where $d(\omega)$ is the photorecombination (PR) transition dipole moment and $W(\omega)$ is the microscopic wave packet. In QRS theory, $W(\omega)$ is determined by the laser field and can be accurately calculated from the SFA, and $d(\omega)$ is the transition dipole between the initial and final states of PR (or PI). When the multielectron effect is not important, the transition dipole can be calculated using the single-active electron (SAE) approximation. However, the transition dipole is easily

generalized to include many-electron effects, as is routinely done in PI theory of atoms and molecules. Thus, to include many-electron effects in $d(\omega)$, multichannel calculations such as many-body perturbation theory, the close-coupling method, the R -matrix method, the random-phase approximation, and many others can all be employed. Since PI of Xe has been well studied, we obtain $d(\omega)$ semiempirically. The major many-body effect for PI of Xe from the $5p$ shell occurs at photon energy where the $4d$ shell is open. Thus, below about 60 eV, the transition dipole from $5p$ can be obtained from a single-electron model. This gives the magnitude and phase of the transition dipole. At higher energies, effects from the $4d$ shell on the transition dipole of $5p$ becomes important since the PI cross section of Xe from $4d$ has a large and broad resonance around 100 eV. The intershell coupling will enhance $d(\omega)$ for $5p$ near and above 90 eV. Such an enhancement has been calculated by Kutzner *et al.* [56] using the relativistic random-phase approximation (RRPA). In our calculation, the phase of $d(\omega)$ is taken from the $5p$ shell under the SAE approximation [32] while the magnitude is taken from Ref. [56]. (A similar procedure was used in Refs. [24] and [27] for the single-atom HHG of Xe.) This approximation does not change the temporal structure of attosecond pulses (shown later) since the phase of $D(\omega)$ is dominated by the phase of the wave packet $W(\omega)$. We comment that, in QRS, the induced dipole is given in the energy domain, thus the calculation is similar to the time-independent theory used in PI which has become well established over the last 30 years.

III. RESULTS AND DISCUSSION

A. Macroscopic HHG spectra of Xe at different laser intensities

HHG spectra of Xe extended to the photon energy of over one hundred electron volts using 1.8 μm lasers with a pulse duration of few optical cycles have been reported recently [38,39].

In Fig. 1, we show the calculated HHG spectra of Xe exposed to a 14 fs (full width at half maximum, or FWHM) 1825 nm laser. The laser beam waist is 100 μm . A 1-mm-long gas jet with a pressure of 30 Torr is placed at the laser focus. The harmonics are detected after a slit with a width of 190 μm and placed 455 mm behind the focus. These parameters are chosen to be close to those in the experiment of Trallero-Herrero *et al.* [39]. For the present purpose we analyze HHG spectra obtained from our theoretical simulations at two laser peak intensities $0.5 \times 10^{14} \text{ W/cm}^2$ and $1.0 \times 10^{14} \text{ W/cm}^2$, which are below and above the critical intensity for Xe at $\sim 0.87 \times 10^{14} \text{ W/cm}^2$ [43], respectively. Here the critical intensity is defined with respect to the static electric field where an electron can classically escape over the top of the field-induced potential barrier.

We first show the single-atom HHG spectra (proportional to $\omega^4 |D(\omega)|^2$ [30]) for CEP = 0 in Fig. 1(a). For clarity, the spectra for high intensity have been shifted up with respect to the low intensity. We can see that the spectra are quite noisy except for the cutoff region for both low and high laser intensities due to the interference between the “short” and “long” electron trajectories and the short laser duration used

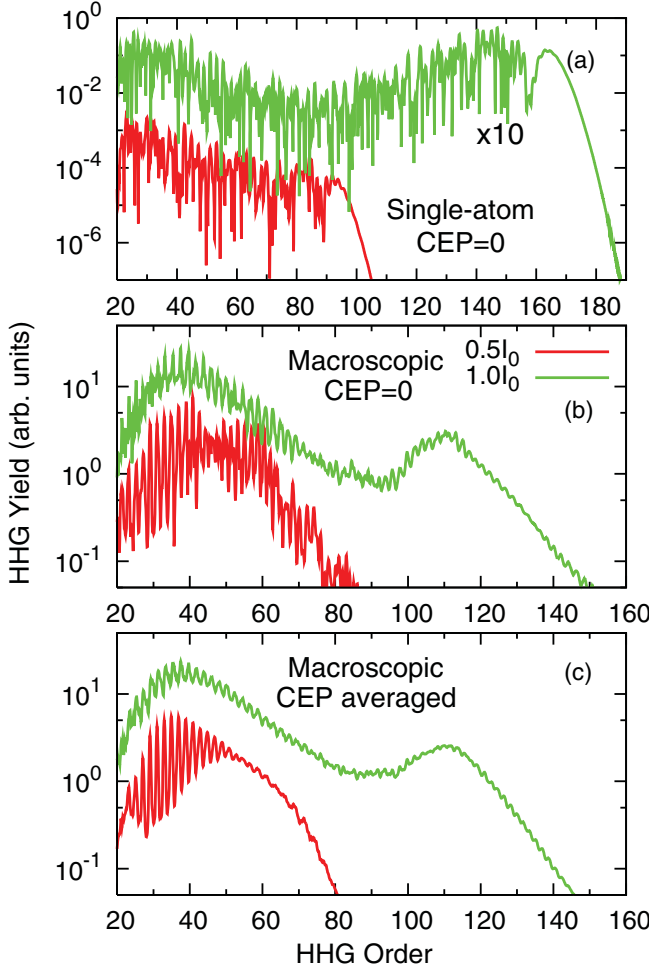


FIG. 1. (Color online) Single-atom and macroscopic HHG spectra of Xe in an 1825 nm laser, for (a), (b) CEP = 0, and (c) CEP averaged. Laser intensities are indicated in units of $I_0 = 10^{14}$ W/cm². See text for additional laser parameters and the experimental arrangement. In (a), the HHG spectra for $1.0I_0$ are multiplied by 10 for clarity.

(see similar spectra for different CEPs in Ref. [27]). We then show the macroscopic HHG spectra for CEP = 0 in Fig. 1(b). The two laser intensities present different characteristics of harmonics, and both are very different from single-atom HHG spectra. For the low intensity, the harmonics are very sharp; that is, the valley between the neighboring odd harmonics (which can only be defined for the low-order harmonics) is very deep. At high intensity, the valley is very shallow (i.e., the spectrum shows a continuum structure). Furthermore, the harmonics are not exactly at odd orders due to the blueshift of the fundamental field. Note that the spectrum rises above about H90 is due to the intershell or many-electron effects discussed in Sec. II C. Since a few-cycle laser pulse is applied, the HHG spectra have a strong CEP dependence. In Fig. 1(c), we show the CEP-averaged macroscopic HHG spectra. The main characteristics of the harmonics remain the same except that the harmonic spectra are much smoother. The CEP is fixed at zero in the following sections unless otherwise stated.

B. Spatiotemporal evolution of fundamental laser field

To understand the different spectral features in Fig. 1, we inspect the fundamental field in the ionizing medium. The spatiotemporal intensity profile and on-axis electric fields of the laser pulse at the entrance and the exit of the gas jet are shown in Fig. 2. The laser peak intensity is 1.0×10^{14} W/cm², which would give an ionization probability of $\sim 35\%$ at the end of laser pulse for Xe, according to an empirical ADK formula in the barrier-suppression regime [43]. While the electric field at the entrance has a good Gaussian shape both in time and space, it is strongly reshaped during propagation in the ionizing medium. At the exit it shows positive chirp in time (blueshift in frequency) [see Fig. 2(c)] and defocusing in space [see Fig. 2(b)]. The depletion of the fundamental electric field makes the cutoff position in Fig. 1(b) much smaller than that in Fig. 1(a). We have also checked the fundamental field with laser peak intensity of 0.5×10^{14} W/cm². It always maintains Gaussian spatial distribution and there is no blueshift because the ionization probability is very low. The reshaping of the fundamental field at high intensity is responsible for the continuum structure in the HHG spectra in Fig. 1. Note that similar results have been obtained by Gaarde *et al.* [18] using a 750 nm laser interacting with Ne gas.

C. Time-frequency analysis of harmonics in near and far fields

Harmonic generation is a temporal coherent process and can be better understood if we study it in terms of its emission time. In this subsection we examine the time-frequency representation (TFR) of harmonics in the near and far fields for the low and high laser intensities.

For each harmonic order q , it is known that the phase can be expressed as [57]:

$$\Phi_i^q(r, z, t) = -\alpha_i^q I(r, z, t), \quad (12)$$

where $I(r, z, t)$ is the spatiotemporal intensity of the fundamental laser field. The proportional constant $\alpha_{i=S, L}$ depends on “short” (S) or “long” (L) trajectories. The phase can also be expressed in terms of the ponderomotive energy U_p and the electron excursion time τ_i^q : $\Phi_i^q \approx -\beta_i U_p \tau_i^q$ [58], where the coefficient β_i for the “short” trajectory is much smaller than for the “long” trajectory. The electron excursion times for the two trajectories are $\tau_S^q \approx T/2$ and $\tau_L^q \approx T$ (T is the laser period) [59]. It shows that the phase grows with the cubic power of the wavelength. The curvature of the phase front caused by the radial variation $\partial \Phi_i^q(r)/\partial r$ makes the harmonic beam divergent. The divergence of “short”- or “long”-trajectory harmonics is determined by either $\Delta \alpha_i^q$ or $\Delta I(r)$.

1. Harmonics in the near field

The TFR, $|A_{\text{near}}(t, \omega)|^2$, calculated from Eq. (8), is shown in Figs. 3(a) and 3(d) for harmonics above H40 at two laser intensities, collected at the exit face of the gas jet (near field). In Fig. 3(a), the symbols S and L are used to indicate the first (earliest) group of harmonics generated. Here S (L) stands for “short”-trajectory (“long”-trajectory) harmonics that have positive (negative) chirp. These harmonics are from electrons born at $t = -1$ (in units of optical cycles); that is, B_{-1} , to

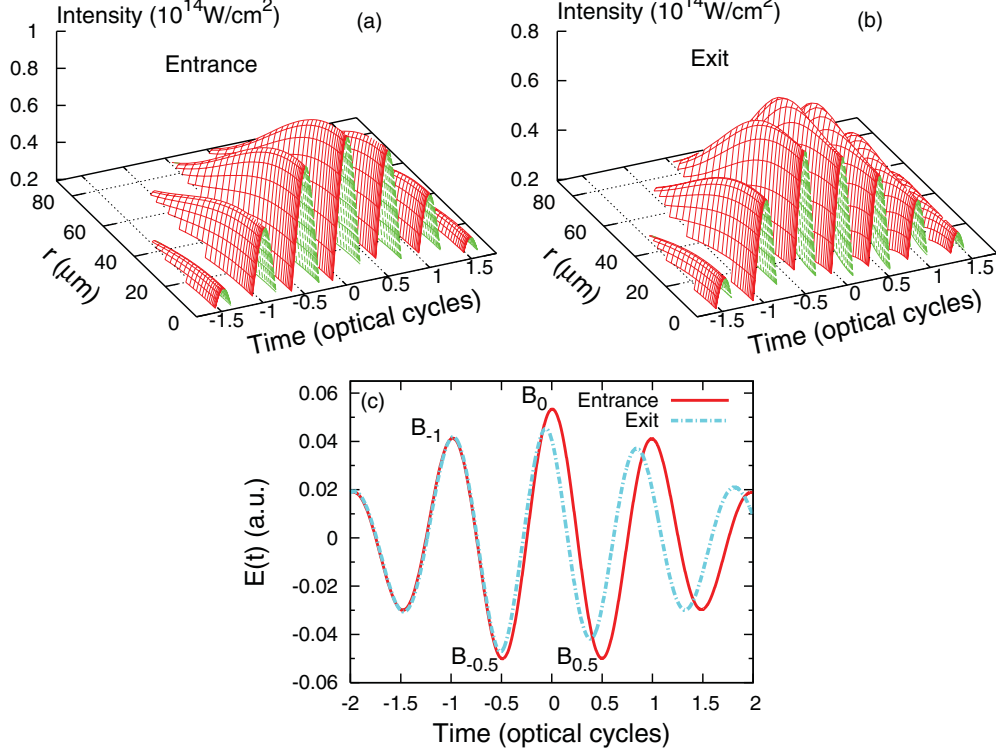


FIG. 2. (Color online) Spatiotemporal intensity profile of the laser pulse at (a) the entrance and (b) the exit of a Xe gas jet. Laser intensity at the focus is $1.0 \times 10^{14} \text{ W/cm}^2$ (assumed in the vacuum) and CEP = 0. (c) Evolution of the on-axis electric field at the entrance (solid line) and the exit (dot-dashed line). The laser field becomes chirped during the propagation. For subcycle dynamics analysis, we use the label B_t , with $t = -1, -0.5, 0$, and 0.5 (in units of optical cycles) to indicate the approximate half cycle where the electron is born. Note that t is defined within the half cycle only.

indicate a birth time at $t = -1$, which is in the leading edge of the pulse [see Fig. 2(c)]. In the following, the electron birth time t (in units of optical cycles) is indicated by B_t in the figure, while the harmonic emission time is read off from the horizontal axis of the figure, one for the “short,” and the other for the “long” trajectory. In this paper the time is always defined in the moving coordinate frame [32]. At the low intensity in Fig. 3(a), we can see that both S and L contribute to harmonics generated from electrons born at $t = -1, -0.5, 0$, and 0.5 . In other words, harmonics are generated by electrons born over four half cycles. Note that Tate *et al.* [60] have shown that harmonics generated by mid-infrared lasers had large contributions from electron trajectories even longer than the “long” trajectories in the single-atom response, which has also been confirmed in our calculation (not shown). But these trajectories are all eliminated during the propagation in the medium since their phases are very large. For low intensity, the propagation in the medium cannot eliminate contributions from “long” trajectories.

The same TFR analysis for the high intensity is shown in Fig. 3(d). Higher harmonic cutoff from each burst is easily seen since the intensity is twice higher. Comparing to Fig. 3(a), there are no contributions to the harmonics from the “long” trajectories for electrons born at $t = -1$ and -0.5 ; that is, from the leading edge of the pulse. Since the laser intensity is twice higher, the phase of each harmonic is also twice higher (see also

Fig. 17 in Ref. [61] and Fig. 1(A) in Ref. [62]), thus resulting in cancellation of contributions from the “long” trajectories. For electrons born at the falling edge of the pulse, due to the blueshift (thus shorter wavelength) and reshaping (thus lower intensity), the phases of the harmonics due to the “long” trajectories are smaller and can survive after propagation in the medium; for example, for electrons born at $t = 0$ and 0.5 ; see Fig. 3(d).

2. On-axis harmonics in the far field

In Fig. 3(b), the TFR is shown for $r = 0$ mm in the far field (455 mm after the laser focus). At low intensity, the emission from “short” trajectories born at different times have the similar small divergence and, after propagation in free space, they all survive along the axis in the far field. Interference between “short”-trajectory harmonics from each half cycle leads to enhancement in odd harmonics and suppression in even harmonics (see Fig. 18 in Ref. [63]) and results in the big contrast between odd harmonics and neighboring harmonics, as shown in Fig. 1(b) for the spectra obtained with a slit. At high intensity, only harmonics from the “short”-trajectory electrons born at $t = -1$ survive (the next one at $t = -0.5$ is much weaker); see Fig. 3(e). This would result in a nearly-continuum spectrum and a potential for generating an isolated attosecond pulse.

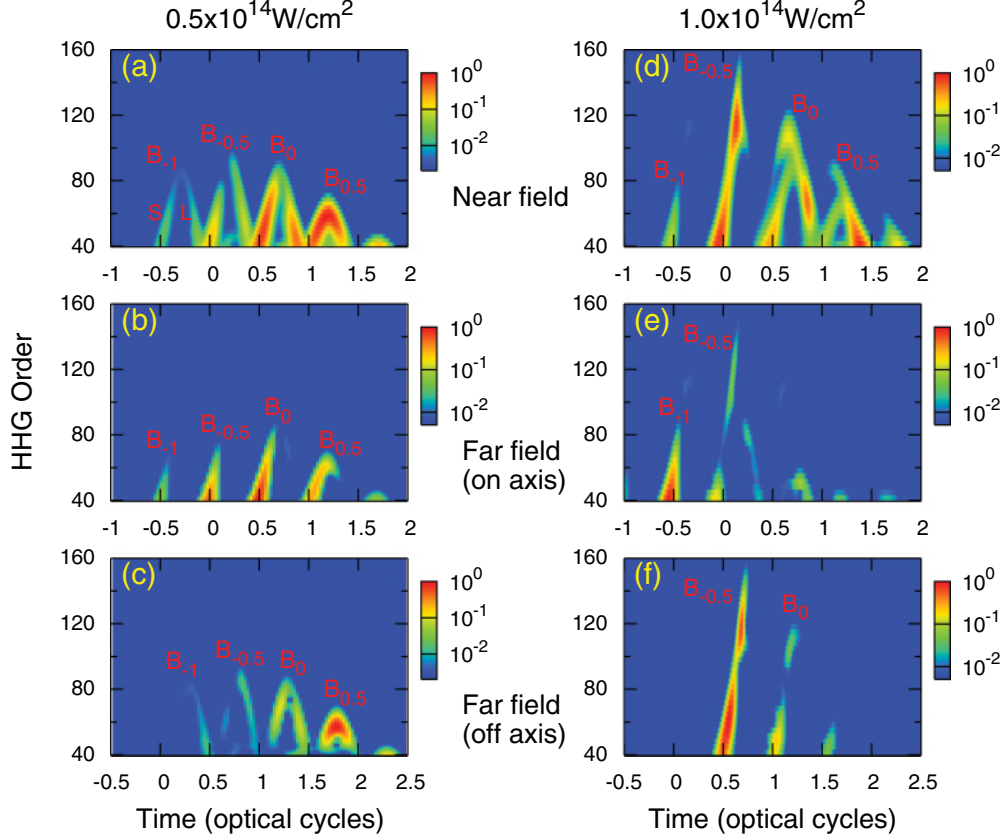


FIG. 3. (Color online) Top row: Time-frequency representation (TFR) of harmonics in the near field. Middle row: TFR for on-axis ($r = 0$ mm, divergence is 0 mrad) harmonics in the far field. Bottom row: TFR for off-axis ($r = 1$ mm, divergence is 2.2 mrad) harmonics in the far field. Far-field position is at $z = 455$ mm, and laser intensity (CEP = 0) along each column is indicated. Electrons are released at each half cycle, labeled by B_t , with $t = -1, -0.5, 0$, and 0.5 as in Fig. 2. For each B_t , electrons can follow a “short” (S) or “long” (L) trajectory to recombine with the ion to emit harmonics. For each harmonic, the emission time can be read from the time axis. For each B_t , the emission time for each off-axis harmonic is delayed with respect to the corresponding on-axis harmonic [e.g., compare (b) vs (c) and (e) vs (f)]. All the TFRs have been normalized.

3. Off-axis harmonics in the far field

In Figs. 3(c) and 3(f), the TFR is shown for $r = 1$ mm (divergence is 2.2 mrad) in the far field. Each off-axis burst has an obvious time delay with respect to the on-axis burst because it travels a longer distance in free space. At low intensity, harmonics from “long” trajectories appear on each burst since they have large divergence [see Fig. 3(c)]. At high intensity, the “short” trajectories contribute to bursts $B_{-0.5}$ and B_0 [see Fig. 3(f)]. They appear to come from the pulse reshaping; see Fig. 2(b) showing laser peak intensity shifting to a region away from the propagation axis. They experience larger $\Delta I(r)$ with respect to “short”-trajectory electrons born at B_{-1} at the leading edge. Figure 3(f) shows that a continuum spectra from a “short” trajectory is generated for electrons born at $t = -0.5$.

Note that attochirp (emission time varying with harmonic order) [62,64] of “short”- or “long”-trajectory harmonics exists even after propagation. They may be compensated using a “plasma compressor” [62] because free electrons induce a negative group velocity dispersion, or by thin filters with linear negative group velocity dispersion [65]. But attochirp is inversely proportional to laser wavelength [66], which implies that one can select a broad range of harmonics to synthesize a short attosecond pulse using an 1825 nm laser (to be shown

next). The harmonic emission of the “short” trajectory in the far field in Figs. 3(e) and 3(f) varies with time or radial distance. This provides possibilities to generate IAPs using different ranges of harmonics on or off axis. In the following, we will only show the spectral and spatial filters applied on axis in the far field.

D. Spectral and spatial filtering in generation of attosecond pulses

A spectral filter is usually used to synthesize attosecond pulses. In this section we also study how the attosecond pulses are manipulated through spatial filtering. Figure 4(a) displays the intensity profile of xuv light by synthesizing H40-H80 at the near field generated by a laser intensity of $0.5 \times 10^{14} \text{ W/cm}^2$. The intensity of the attosecond pulses $I_{\text{near}}(t)$ is calculated by using Eq. (9). The time-frequency analysis of these harmonics has been given in Fig. 3(a). Besides attosecond bursts occurring at each half optical cycle, which can be attributed to harmonics resulting from “short” trajectories, we observe other pulses in between which are attributed to contributions from “long” trajectories. The main peaks from the “short” trajectories are labeled 1, 3, 5, and 7 in the figure, while those in between (2, 4, 6, and 8) are not

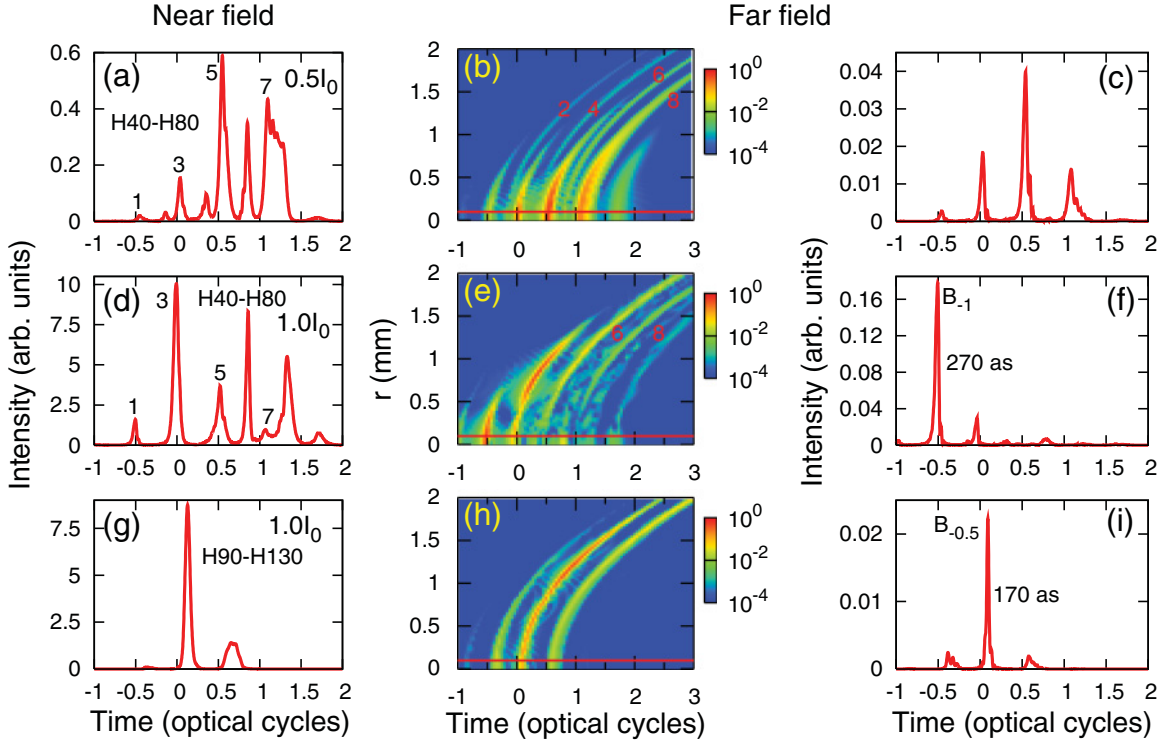


FIG. 4. (Color online) First column: Intensity (or envelope) of attosecond pulses in the near field, synthesized from the harmonics and the laser intensity shown in each frame. Laser intensities are given in units of $I_0 = 10^{14} \text{ W/cm}^2$. In (a) and (d), odd bursts (“short” trajectories) are labeled. Even bursts due to “long” trajectories are not labeled, for brevity. Middle column: Spatial distribution (normalized) of attosecond pulses in the far field ($z = 455 \text{ mm}$). Notice that even bursts (“long” trajectories) have large divergence, or at large r . The odd bursts (not labeled) have smaller divergence. There is a time delay between off-axis attosecond pulses compared to on-axis ones. Last column: Intensity of attosecond pulses in the far field using a spatial filter with a radius $r_0 = 100 \mu\text{m}$ (shown by the solid line in red in each middle-column frame). In (f) and (i), the main emission bursts are labeled with the electron birth times B_t for $t = -1$ and -0.5 , respectively.

labeled) are from “long” trajectories. The attosecond pulses thus generated show a poor periodicity in time; see Fig. 4(a).

If the xuv light is synthesized in the far field, in particular, by introducing a spatial filter, then it may be possible to remove harmonics resulting from the “long” trajectories. In Fig. 4(b), the intensity distributions of the synthesized light in space in the far field are shown. They are obtained from the near-field harmonics by further propagation in free space. The peaks 2, 4, 6, and 8 [not explicitly shown in Fig. 4(a)] are attributed to “long” trajectories. They are indicated in Fig. 4(b) showing that they are distributed far from the propagation axis. By using a spatial filter (indicated by a solid line in red, with a radius $r_0 = 100 \mu\text{m}$) to select harmonics generated near the axis only, as shown in Fig. 4(c) by using Eq. (10) to calculate $I_{\text{far}}(t)$, well-behaved APTs are then obtained. We comment that the time delay between off-axis and on-axis harmonics leads to the curved spatial distribution in Fig. 4(b) and can be understood mathematically since each harmonic behaves like a Gaussian beam, and the geometric phase of each harmonic is proportional to r^2 along the transverse direction (see Fig. 4 in Ref. [32]). The traveling distance of off-axis harmonics can be compensated using a reflecting mirror to refocus the harmonic beam or by a detector with a curved surface. In principle, this compensation becomes important to reduce the duration of attosecond pulses when a spatial filter with a large radius is applied. In this paper, the radius of the spatial filter is chosen to be small enough to avoid this curvature effect.

Next we use the same range of harmonics (H40-H80) generated by the laser intensity of $1.0 \times 10^{14} \text{ W/cm}^2$ to synthesize attosecond pulses in the near field. Referring to Fig. 3(b), the “short” trajectories dominate the harmonic generation in the leading edge of the laser, while the “long” trajectories dominate the harmonic generation in the falling edge. The synthesized xuv light, shown in Fig. 4(d) indeed reflects this point where the first two peaks occur at multiples of half optical cycles, while the last four peaks do not. In Fig. 4(e), the spatial distribution of the synthesized xuv light in the far field indeed supports this description. By using a spatial filter (indicated by a solid red line with a radius $r_0 = 100 \mu\text{m}$) to select only “short” trajectories, as shown in Fig. 4(f), a nice IAP with a duration of 270 as is obtained, accompanied by a weak subpulse with a much weaker intensity. This demonstrates the generation of IAPs using spatial filtering. A similar mechanism of IAP generation has been proposed by Strelkov *et al.* [67,68] using the harmonics in the plateau region generated by Ar gas with very high pressure.

The TFR in Fig. 3(e) shows considerable on-axis emission above H80 at burst $B_{-0.5}$. We use H90-H130 to generate attosecond pulses in the near field in Fig. 4(g). Both bursts have considerable contributions from “short” trajectories. In the far field [see Fig. 4(h)], they show different divergences as discussed before. Finally, we obtain an IAP with a duration of about 170 as in Fig. 4(i) with a spatial filter. The intensity of the IAP is about 1/8 that in Fig. 4(f), due not only to

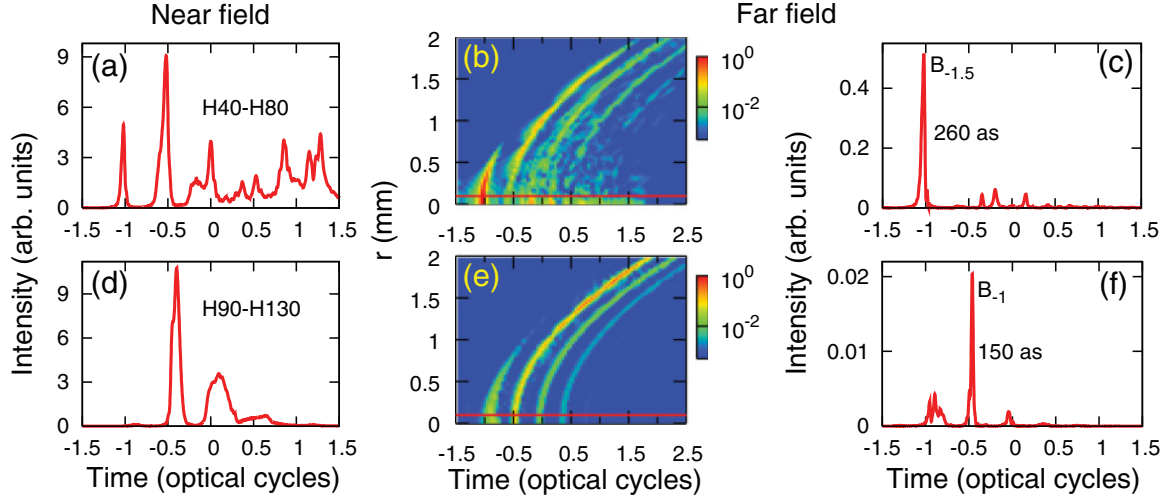


FIG. 5. (Color online) Top row: Attosecond pulses synthesized from H40-H80 (a) at the near field, (b) its spatial distribution at the far field ($z = 455$ mm), and (c) a good isolated attosecond pulse generated if a filter with a radius $r_0 = 100 \mu\text{m}$ is used to select only near-axis harmonics (indicated by a solid red line in the middle frame). Bottom row: Attosecond pulses synthesized from H90-H130; (d), (e), and (f) are similar to (a), (b), and (c). The birth times for the bursts that generate the IAP for H40-80 and for H90-130 are indicated by B_t for $t = -1.5$ and -1 , respectively. Laser intensity is $2.0 \times 10^{14} \text{ W/cm}^2$ and CEP = 0.

the larger divergence of “short”-trajectory harmonics born at $B_{-0.5}$ compared with those born at B_{-1} , but also to the lower harmonic intensity of H90-H130 compared with H40-H80. On the other hand, the duration of the IAP is decreased. A similar mechanism of IAP generation has been proposed by Gaarde *et al.* [17,18] using harmonics in the cutoff region by a 750 nm laser irradiating Ne gas.

We next check how the IAP generation works at higher intensities; say at $2.0 \times 10^{14} \text{ W/cm}^2$. Figure 5 should be compared with Figs. 4(d)–4(i) directly. For the synthesized H40-H80 pulse, Fig. 5(a) shows that the harmonics are emitted about half an optical cycle earlier than the one at half the intensity ($1.0 \times 10^{14} \text{ W/cm}^2$). Figure 5(b) shows that the pulses generated at the falling edge of the laser pulse have large divergence and thus tend to come from “long” trajectories. In fact, this portion of the pulse does not have good periodic time dependence. Figure 5(b) also shows that only the pulse emitted at $t = -1$ (in units of optical cycles) is near the axis, thus a filter selecting near-axis harmonics results in an IAP, as illustrated in Fig. 5(c). The IAP has a duration of 260 as. For pulses synthesized from H90-H130, Fig. 5(d) shows that there are two bursts emitted at $t = -0.5$ and 0, and their lateral profiles in the far field are shown in Fig. 5(e). By using a filter, an attosecond pulse of 150 as can be obtained. In this case, the IAP intensity does not increase since the fundamental laser field is much reshaped and the harmonic has a much bigger divergence in the far field in comparison with $1.0 \times 10^{14} \text{ W/cm}^2$. It is concluded that ionization gating still works at a higher laser intensity, and it is more efficient to select bursts that are born in the leading edge before the laser field starts to be depleted and blueshifted.

Another question that arises is whether the strength of attosecond pulses can be improved by increasing gas pressure. For “weak” fields and low pressure, Shiner *et al.* [69] have shown experimentally that the harmonic yield increases quadratically with the pressure. For “high” fields addressed

here, laser pulse reshaping is important, we have confirmed theoretically that increasing the gas pressure while maintaining the same intensity would not always increase the harmonic yields of Ar [70]. On the other hand, the pressure effect on the high harmonics of Xe at “high” field has been studied in Ref. [39]. But its effect on the attosecond pulse was not examined in this paper.

E. Far-field position dependence of isolated attosecond pulses

The position of the spatial filter in the far field can be easily adjusted in an experiment. Here we show the change of attosecond pulses with the far-field position. In Fig. 6, attosecond pulses synthesized (H40-H80) at two other positions $z = 100$ mm and 900 mm are given. This is to be compared with the ones at $z = 455$ mm in Figs. 4(e) and 4(f). Using the same filter (indicated by the solid red line for fixed $r_0 = 100 \mu\text{m}$), the attosecond pulses generated are shown in Figs. 6(b) and 6(d). The width of the main burst does not change much with z , but the strength of the satellite peak is reduced. Of course this is achieved at the expense of decreasing the strength of the attosecond pulse. This has also been shown by Gaarde and Schafer [17] where an IAP was selected by moving the reflecting mirror further from the laser focus.

F. Comparison between QRS and SFA in modeling propagation effect

In the last two decades, the strong-field approximation (SFA), which is in the frame of the SAE approximation, has been widely used to predict the temporal structure of attosecond pulses even though SFA is unable to explain the observed harmonic spectra precisely in general. In the present calculation, we use QRS in the propagation calculation. For the single-atom response, QRS has been tested against TDSE both for the magnitude and phase, as documented in Le *et al.* [55], for example. In QRS, the wave packet is obtained

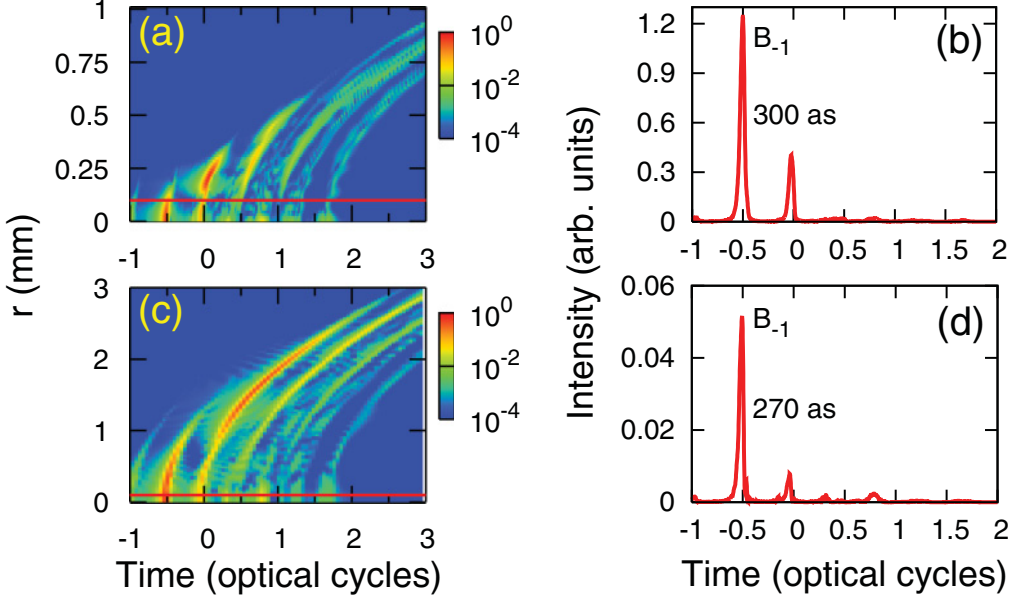


FIG. 6. (Color online) Dependence of attosecond pulse generation on the filter position in the far field. Spatial distribution [(a) and (c)] (normalized) and attosecond pulses synthesized [(b) and (d)] at different far-field positions: $z = 100$ mm (top row) and $z = 900$ mm (bottom row), using H40-H80. Laser intensity is 1.0×10^{14} W/cm 2 . These figures are to be compared to Figs. 4(e) and 4(f) for $z = 455$ mm. Intensity of attosecond pulses in the far field is obtained using a spatial filter with a fixed radius $r_0 = 100$ μm [indicated by the solid red line in (a) and (c)]. The main emission burst is labeled with the electron birth time $t = -1$, or B_{-1} . The calculation is for CEP = 0.

from the SFA, including the phase. The transition dipole $d(\omega)$ in Eq. (11), also introduces a phase. In the SFA, this phase is a constant, either real or pure imaginary (depending on the symmetry of the ground state), and is independent of harmonic order. In QRS, the transition dipole moment is a complex number in general. From PI theory, however, it is known that the phase of the transition dipole does not change much with photon energy. Thus the phases of the harmonics calculated from QRS and SFA do not differ significantly. Since the phases of the harmonics are much more important in synthesizing attosecond pulses [71], this explains why propagation theory

based on the SFA has been so successful in explaining the generation of attosecond pulses, in spite of its failure in predicting or explaining the observed harmonic spectra. In this subsection, we support this analysis with actual results from simulations.

In Fig. 7(a) the HHG spectra of Xe obtained from the SFA (within the SAE approximation) and QRS (including multi-electron effects) using the laser parameters given in the captions are shown. Clearly the spectra differ greatly. In Figs. 7(b) and 7(c) the synthesized (H40-H80) attosecond pulses at the near field and the far field are shown. Clearly the results from

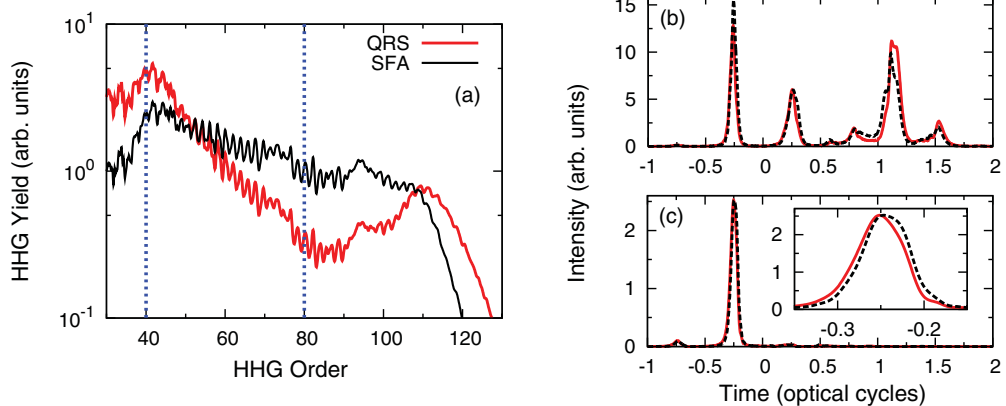


FIG. 7. (Color online) Comparison of HHG spectra and attosecond pulses calculated using QRS and the SFA for single-atom-induced dipoles. (a) Macroscopic HHG spectra (total spectra without using a slit) of Xe by QRS [red (dark gray) line] and the SFA [black (light gray) line]. Laser parameters: $I = 1.0 \times 10^{14}$ W/cm 2 and CEP = $\pi/2$. Intensity of attosecond pulses (b) in the near field and (c) in the far field ($z = 455$ mm) using a spatial filter with a radius $r_0 = 300$ μm : QRS [red (solid) lines] vs the SFA [black (dashed) lines]. Inset in (c) shows enlarged temporal structure of an IAP. The spectra are normalized at the peak intensities in (c). The same normalization factor is used in (a) and (b). H40-H80 are used to synthesize attosecond pulses.

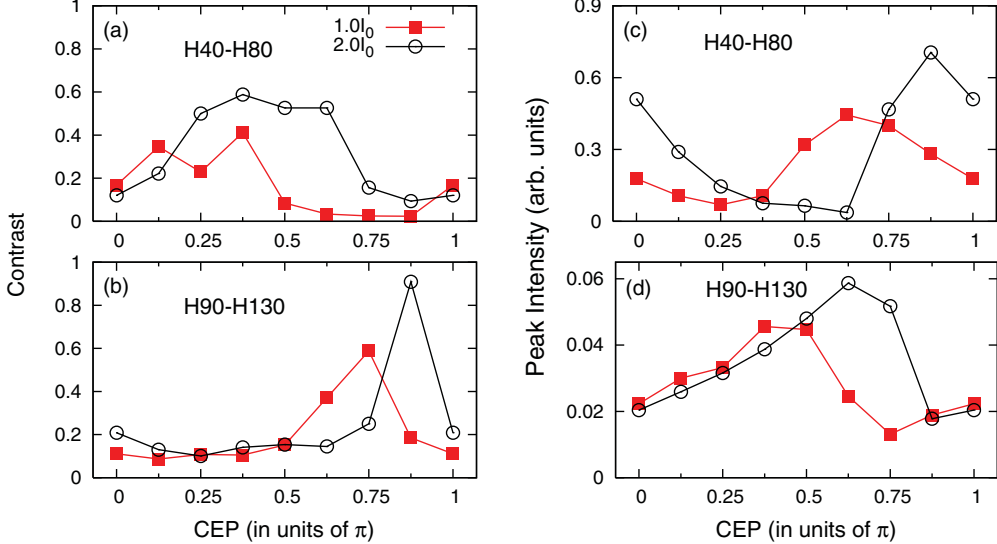


FIG. 8. (Color online) (a), (b) Contrast ratio between the intensities of the strongest satellite and the main attosecond burst. (c), (d) The peak intensity of the main attosecond burst as a function of CEP. Laser intensities are shown in units of $I_0 = 10^{14} \text{ W/cm}^2$. Harmonics used to generate the IAP are labeled. Far-field position is $z = 455 \text{ mm}$, and the radius of the spatial filter is $r_0 = 100 \mu\text{m}$.

the two calculations are essentially identical (after an overall normalization), in spite of the large differences in the harmonic spectra. We have checked some other cases and found that the temporal structures of the attosecond pulses from the two theories are always very similar. Larger differences than those shown in Figs. 7(b) and 7(c) are expected if a wider range of harmonics is used or if the spectra from the two theories differ much more, but the general conclusion is correct.

G. CEP dependence of isolated attosecond pulses

The selection of an IAP by a spatial filter in the far field discussed above is only for a single CEP and thus is only useful if the laser is CEP stabilized (which has not been achieved yet for $1.8 \mu\text{m}$ lasers). To check if the method can be used for lasers that are not CEP stabilized, we investigate the CEP dependence of the IAP generation.

In Figs. 8(a) and 8(b), we show the contrast ratio between the intensities of the strongest satellite and the strongest attosecond burst and, in Figs. 8(c) and 8(d), we show the peak intensity of the strongest attosecond burst as the CEP is varied for the two laser intensities indicated. A good IAP is to have high peak intensity for the main peak and weak satellites. From Figs. 8(c) and 8(d), we note that, at the CEPs where the strongest attosecond bursts have high peak values, the contrast ratios shown in Figs. 8(a) and 8(b) are always small. In the meanwhile, when the contrast ratio is large, the strongest attosecond burst is always weak. Thus it is possible to generate single attosecond pulses even when the CEP of the driving laser is not stabilized. This explains the success why the first single attosecond pulses were generated using few-cycle laser pulses that were not phase-stabilized [16].

IV. CONCLUSIONS

In this paper, we have studied the generation of isolated attosecond pulses (IAPs) using few-cycle mid-infrared lasers

at large intensities near and above the critical intensity of Xe. The calculations are based on QRS theory where many-electron effects are included in the single-atom-induced dipole moment; specifically, by including the coupling of the inner $4d$ shell of Xe in the partial $5p$ photorecombination transition dipole matrix element. The effect of the medium on the fundamental and harmonic fields is obtained by solving the Maxwell wave equations. The modification (or reshaping in space and time) of the fundamental field is due to its nonlinear interaction with the medium and includes dispersion, the plasma effect, and the Kerr nonlinearity. We have investigated the spatiotemporal evolution of the fundamental laser field in detail and found that its reshaping is responsible for the continuum structure in the HHG spectra. This conclusion is carried out in terms of the time-frequency analysis of harmonics in the near and far fields.

Since the divergence of harmonic emission from different half cycles is varied due to the blueshift and defocusing of the fundamental laser pulse (or complicated reshaping), we have shown that isolated attosecond pulses can be generated by synthesizing H40-H80 or H90-H130, selected by a spatial filter centered on the propagation axis in the far field. The mechanism of IAP generation in this paper could be called as “ionization gating.” It works for a loosely focused laser at high laser intensity (above the critical intensity), which is reshaped as it propagates through the medium with a moderate gas pressure. A similar approach has been discussed by Gaarde *et al.* [17,18] using a 750 nm laser interacting with 135 Torr Ne gas. We have found that it is easier to reshape the fundamental field using a long-wavelength laser with a moderate gas pressure (~ 30 Torr). The extended harmonic cutoff of Xe leads to a broad range of harmonics available for IAP generation. This approach is also different from Ferrari *et al.* [36] where low harmonics (~ 30 eV, which is equivalent to H40 in this paper) are used to generate the IAP. In addition, we have discussed the possibilities of improving the intensity

of the IAP, such as changing the far-field position, increasing the laser intensity, and increasing gas pressure. We have shown that the method is very robust and an IAP can be generated even if the laser CEP is not stabilized.

ACKNOWLEDGMENTS

This work was supported in part by the Chemical Sciences, Geosciences, and Biosciences Division, Office of Basic Energy Sciences, Office of Science, US Department of Energy.

-
- [1] F. Krausz and M. Ivanov, *Rev. Mod. Phys.* **81**, 163 (2009).
- [2] M. Nisoli and G. Sansone, *Prog. Quantum Electron.* **33**, 17 (2009).
- [3] P. Agostini and L. F. DiMauro, *Rep. Prog. Phys.* **67**, 813 (2004).
- [4] M. B. Gaarde, J. L. Tate, and K. J. Schafer, *J. Phys. B* **41**, 132001 (2008).
- [5] T. Popmintchev, M.-C. Chen, P. Arpin, M. M. Murnane, and H. C. Kapteyn, *Nat. Photonics* **4**, 822 (2010).
- [6] I. P. Christov, M. M. Murnane, and H. C. Kapteyn, *Phys. Rev. Lett.* **78**, 1251 (1997).
- [7] E. Goulielmakis *et al.*, *Science* **320**, 1614 (2008).
- [8] G. Sansone *et al.*, *Science* **314**, 443 (2006).
- [9] H. Mashiko, S. Gilbertson, C. Li, S. D. Khan, M. M. Shakya, E. Moon, and Z. Chang, *Phys. Rev. Lett.* **100**, 103906 (2008).
- [10] C. A. Haworth, L. E. Chipperfield, J. S. Robinson, P. L. Knight, J. P. Marangos, and J. W. G. Tisch, *Nat. Phys.* **3**, 52 (2007).
- [11] T. Pfeifer, A. Jullien, M. J. Abel, P. M. Nagel, L. Gallmann, D. M. Neumark, and S. R. Leone, *Opt. Express* **15**, 17120 (2007).
- [12] I. Thomann, A. Bahabad, X. Liu, R. Trebino, M. M. Murnane, and H. C. Kapteyn, *Opt. Express* **17**, 4611 (2009).
- [13] C. Liu, R. Li, Z. Zeng, Y. Zheng, P. Liu, and Z. Xu, *Opt. Lett.* **35**, 2618 (2010).
- [14] C. Liu, Y. Zheng, Z. Zeng, R. Li, and Z. Xu, *Phys. Rev. A* **79**, 043826 (2009).
- [15] Y. Zheng, Z. Zeng, H. Xiong, R. Li, Z. Xu, Y. Peng, X. Yang, and H. Zeng, *Appl. Phys. Lett.* **95**, 141102 (2009).
- [16] M. Hentschel, R. Kienberger, Ch. Spielmann, G. A. Reider, N. Milosevic, T. Brabec, P. Corkum, U. Heinzmann, M. Drescher, and F. Krausz, *Nature (London)* **414**, 509 (2001).
- [17] M. B. Gaarde and K. J. Schafer, *Opt. Lett.* **31**, 3188 (2006).
- [18] M. B. Gaarde, M. Murakami, and R. Kienberger, *Phys. Rev. A* **74**, 053401 (2006).
- [19] M. Lewenstein, Ph. Balcou, M. Yu. Ivanov, A. L'Huillier, and P. B. Corkum, *Phys. Rev. A* **49**, 2117 (1994).
- [20] C. D. Lin, A. T. Le, Z. Chen, T. Morishita, and R. R. Lucchese, *J. Phys. B* **43**, 122001 (2010).
- [21] T. Morishita, A. T. Le, Z. Chen, and C. D. Lin, *Phys. Rev. Lett.* **100**, 013903 (2008).
- [22] A. T. Le, R. R. Lucchese, S. Tonzani, T. Morishita, and C. D. Lin, *Phys. Rev. A* **80**, 013401 (2009).
- [23] M. V. Frolov, N. L. Manakov, T. S. Sarantseva, and A. F. Starace, *J. Phys. B* **42**, 035601 (2009).
- [24] M. V. Frolov, N. L. Manakov, T. S. Sarantseva, M. Yu. Emelin, M. Yu. Ryabikin, and A. F. Starace, *Phys. Rev. Lett.* **102**, 243901 (2009).
- [25] M. V. Frolov, N. L. Manakov, and A. F. Starace, *Phys. Rev. A* **79**, 033406 (2009).
- [26] M. V. Frolov, N. L. Manakov, T. S. Sarantseva, and A. F. Starace, *Phys. Rev. A* **83**, 043416 (2011).
- [27] M. V. Frolov, N. L. Manakov, A. A. Silaev, N. V. Vvedenskii, and A. F. Starace, *Phys. Rev. A* **83**, 021405 (2011).
- [28] A. Čerkić, E. Hasović, D. B. Milošević, and W. Becker, *Phys. Rev. A* **79**, 033413 (2009).
- [29] O. I. Tolstikhin, T. Morishita, and S. Watanabe, *Phys. Rev. A* **81**, 033415 (2010).
- [30] C. Jin, A. T. Le, and C. D. Lin, *Phys. Rev. A* **79**, 053413 (2009).
- [31] C. Jin, H. J. Wörner, V. Tosa, A. T. Le, J. B. Bertrand, R. R. Lucchese, P. B. Corkum, D. M. Villeneuve, and C. D. Lin, *J. Phys. B* **44**, 095601 (2011).
- [32] C. Jin, A. T. Le, and C. D. Lin, *Phys. Rev. A* **83**, 023411 (2011).
- [33] C. Jin, A. T. Le, and C. D. Lin, *Phys. Rev. A* **83**, 053409 (2011).
- [34] S. F. Zhao, C. Jin, R. R. Lucchese, A. T. Le, and C. D. Lin, *Phys. Rev. A* **83**, 033409 (2011).
- [35] E. J. Takahashi, P. Lan, O. D. Mücke, Y. Nabekawa, and K. Midorikawa, *Phys. Rev. Lett.* **104**, 233901 (2010).
- [36] F. Ferrari, F. Calegari, M. Lucchini, C. Vozzi, S. Stagira, G. Sansone, and M. Nisoli, *Nat. Photonics* **4**, 875 (2010).
- [37] C. Vozzi, M. Negro, F. Calegari, S. Stagira, K. Kovács, and V. Tosa, *New J. Phys.* **13**, 073003 (2011).
- [38] A. D. Shiner, B. E. Schmidt, C. Trallero-Herrero, H. J. Wörner, S. Patchkovskii, P. B. Corkum, J.-C. Kieffer, F. Légaré, and D. M. Villeneuve, *Nat. Phys.* **7**, 464 (2011).
- [39] C. Trallero-Herrero, C. Jin, B. E. Schmidt, A. D. Shiner, J.-C. Kieffer, P. B. Corkum, D. M. Villeneuve, C. D. Lin, F. Légaré, and A. T. Le, e-print arXiv:1110.0865v1.
- [40] E. Takahashi, V. Tosa, Y. Nabekawa, and K. Midorikawa, *Phys. Rev. A* **68**, 023808 (2003).
- [41] M. Geissler, G. Tempea, A. Scrinzi, M. Schnürer, F. Krausz, and P. Brabec, *Phys. Rev. Lett.* **83**, 2930 (1999).
- [42] S. C. Rae and K. Burnett, *Phys. Rev. A* **46**, 1084 (1992).
- [43] X. M. Tong and C. D. Lin, *J. Phys. B* **38**, 2593 (2005).
- [44] E. Priori *et al.*, *Phys. Rev. A* **61**, 063801 (2000).
- [45] V. Tosa, H. T. Kim, I. J. Kim, and C. H. Nam, *Phys. Rev. A* **71**, 063807 (2005).
- [46] B. L. Henke, E. M. Gullikson, and J. C. Davis, *At. Data Nucl. Data Tables* **54**, 181 (1993).
- [47] A. E. Siegman, *Lasers* (University Science, Mill Valley, 1986).
- [48] V. Tosa, K. T. Kim, and C. H. Nam, *Phys. Rev. A* **79**, 043828 (2009).
- [49] L. E. Chipperfield, J. S. Robinson, P. L. Knight, J. P. Marangod, and J. W. G. Tisch, *Laser Photonics Rev.* **4**, 697 (2010).
- [50] X. M. Tong and Shih-I. Chu, *Phys. Rev. A* **61**, 021802 (2000).
- [51] M. B. Gaarde, Ph. Antoine, A. L'Huillier, K. J. Schafer, and K. C. Kulander, *Phys. Rev. A* **57**, 4553 (1998).
- [52] M. B. Gaarde, *Opt. Express* **8**, 529 (2001).
- [53] V. S. Yakovlev and A. Scrinzi, *Phys. Rev. Lett.* **91**, 153901 (2003).

- [54] Ph. Antoine, A. L'Huillier, and M. Lewenstein, *Phys. Rev. Lett.* **77**, 1234 (1996).
- [55] A. T. Le, T. Morishita, and C. D. Lin, *Phys. Rev. A* **78**, 023814 (2008).
- [56] M. Kutzner, V. Radojević, and H. P. Kelly, *Phys. Rev. A* **40**, 5052 (1989).
- [57] M. B. Gaarde, F. Salin, E. Constant, Ph. Balcou, K. J. Schafer, K. C. Kulander, and A. L'Huillier, *Phys. Rev. A* **59**, 1367 (1999).
- [58] A. Zaïr *et al.*, *Phys. Rev. Lett.* **100**, 143902 (2008).
- [59] M. Lewenstein, P. Salières, and A. L'Huillier, *Phys. Rev. A* **52**, 4747 (1995).
- [60] J. Tate, T. Auguste, H. G. Muller, P. Salières, P. Agostini, and L. F. DiMauro, *Phys. Rev. Lett.* **98**, 013901 (2007).
- [61] G. Sansone, C. Vozzi, S. Stagira, and M. Nisoli, *Phys. Rev. A* **70**, 013411 (2004).
- [62] Y. Mairesse *et al.*, *Science* **302**, 1540 (2003).
- [63] M. Protopapas, C. H. Keitel, and P. L. Knight, *Rep. Prog. Phys.* **60**, 389 (1997).
- [64] Y. Mairesse *et al.*, *Phys. Rev. Lett.* **93**, 163901 (2004).
- [65] R. López-Martens *et al.*, *Phys. Rev. Lett.* **94**, 033001 (2005).
- [66] G. Doumy, J. Wheeler, C. Roedig, R. Chirla, P. Agostini, and L. F. DiMauro, *Phys. Rev. Lett.* **102**, 093002 (2009).
- [67] V. Strelkov, E. Mével, and E. Constant, *Eur. Phys. J. Special Topics* **175**, 15 (2009).
- [68] V. V. Strelkov, E. Mével, and E. Constant, *New J. Phys.* **10**, 083040 (2008).
- [69] A. D. Shiner, C. Trallero-Herrero, N. Kajumba, H.-C. Bandulet, D. Comtois, F. Légaré, M. Giguère, J.-C. Kieffer, P. B. Corkum, and D. M. Villeneuve, *Phys. Rev. Lett.* **103**, 073902 (2009).
- [70] G. Wang, C. Jin, A. T. Le, and C. D. Lin, e-print arXiv:1107.6018v1.
- [71] M. B. Gaarde and K. J. Schafer, *Phys. Rev. Lett.* **89**, 213901 (2002).